

# Determination of Special Boundary Coordination at Quadruple Nodes using EBSD

By

Christopher Ng

Submitted to the Department of Materials  
Science and Engineering in  
Partial Fulfillment of the Requirements for the  
Degree of

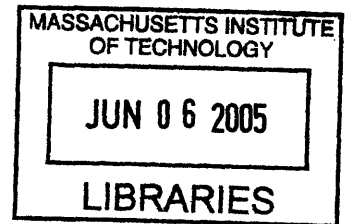
Bachelor of Science

at the

Massachusetts Institute of Technology

June 2005

© Christopher Ng  
All rights reserved



The author hereby grants to MIT permission to reproduce and to  
distribute publicly paper and electronic copies of this thesis document in whole or in part.

Signature of Author: .....  
Department of Materials Science and Engineering  
May 13<sup>th</sup>, 2005

Certified By: .....  
Christopher A. Schuh  
Dane and Vasilios Salapatas Assistant Professor of Metallurgy  
Thesis Supervisor

Accepted By: .....  
Donald R. Sadoway  
John F. Elliott Professor of Materials Chemistry  
Chair, Undergraduate Thesis Committee

**ARCHIVES**

# Determination of Special Boundary Coordination at Quadruple Nodes using EBSD

by

Christopher Ng

Submitted to the Department of Materials Science and Engineering  
on May 13, 2005 in Partial Fulfillment of the Requirements for the Degree of  
Bachelor of Science in Materials Science and Engineering

## **Abstract**

Grain boundaries are known to play an important role in materials properties including corrosion and cracking resistance. Some grain boundaries are resistant to corrosion and cracking and are known as “special” boundaries. While the structure of individual grain boundaries is important, the connectivity of the grain boundaries largely determines the properties of a bulk material. The coordination and connectivity of special grain boundaries have previously been studied in two dimensional grain boundary networks and are quantified by the triple junction distribution (TJD), which has been found to be non-random. The study of connectivity has been extended to three dimensions and simulations have previously been done to obtain a quadruple node distribution (QND) which was also non-random. Using Electron Back-Scattered Diffraction to characterize grain boundaries in copper and aluminum, this project obtains an experimental quadruple node distribution and verifies that it too is non-random.

Thesis Supervisor: Christopher A. Schuh

Title: Danae and Vasilios Salapatias Assistant Professor of Metallurgy

## Table of Contents

Abstract .....	1
List of Figures.....	3
1. Introduction .....	5
2. Method for Obtaining Quadruple Node Information from 2D Sections.....	12
3. Experimental Procedure.....	12
3.1 Specimen Preparation.....	12
3.2 Analysis of Quadruple Nodes.....	15
4. Discussion.....	16
4.1 Analysis of Aluminum.....	17
4.2 Analysis of Copper.....	17
5. Conclusions.....	19
6. Future Work.....	19
Reference.....	21

## List of Figures

- Figure 1: (a) An OIM map of a copper microstructure. The different colors correspond to different grain orientations as indicated in the inverse pole figure below the OIM scan. (b) The same map of a copper microstructure but with only the grain boundaries shown.
- Figure 2: A schematic grain boundary network where each hexagon represents a different grain and each line a grain boundary. A triple junction, the point where three grain boundaries meet, is circled in blue. The green lines highlight the special boundaries and the red lines represent a crack propagating across the grain boundary network. The crack is arrested when it reaches a triple junction with two special grain boundaries.
- Figure 3: There are 4 different types of triple junctions, classified as  $J_i$ , where  $i$  ( $=0$  to  $3$ ) represents the number of special boundaries in the triple junction. The maroon and green lines represent general and special grain boundaries, respectively.
- Figure 4: Triple junction distributions as determined by Frary and Schuh for random microstructure (black lines), existing experimental data (points), fiber textured simulations (green), and general textured simulations (purple) [15].
- Figure 5: (a) A schematic illustration of a quadruple node, the point where four grains, six grain boundaries, and four triple junctions meet. Each grain is labeled  $G_i$  ( $i = 0$  to  $3$ ) and some of the boundaries are labeled with lower case letters. (b) The same quadruple node as in (a), where the planes (labeled a – f) are the grain boundaries and the thick black lines are the triple junctions. (c) Representation of the quadruple node where the lines are the grain boundaries (labeled a –f) and the vertices are triple junctions. The grains are the areas between the lines; the grain labels and colors are the same as those in part (a).
- Figure 6: The 11 different types of quadruple nodes, labeled  $Q_{ij}$ , where  $i$  ( $= 0$  to  $6$ ) is the number of special boundaries in the triple junction and  $j$  ( $= 0$  to  $4$ ) is the number of triple junctions coordinated by at least two special boundaries. The thick green lines represent special boundaries while the black lines represent general boundaries.
- Figure 7: (a) Schematic of a quadruple node shown in Figure 5b. (b) Triple junction formed from grain boundaries a, b, and c. This is what one would see if one sectioned Figure 7a at red dot. (c) Optical micrograph of copper outlined. A triple junction is outlined in green while the blue outlines show other grains in picture. (d) Schematic of a quadruple node shown in Figure 5b. (e) Three sided grain one would see if sectioned Figure 7d at purple dot. (f) The three sided is grain outlined in green while the blue outlines show matching grains from Figure 7c.
- Figure 8: Optical micrograph of copper. The black marks in the corners are Vicker's indents (labeled 1 through 3), which were used as fiducial markers. Several three-sided grains have been identified and are outlined in black (labeled a-d).

Figure 9: Optical micrograph of pure aluminum. Several three-sided grains have been identified and are circled in yellow (labeled a-c).

Figure 10: An OIM map of a three-sided grain. The different colors correspond to different grain orientations and are shown in the inverse pole figure beside the OIM scan. A particular point is shaded in the OIM scan according to the alignment of these three directions in the crystal.

Figure 11: An OIM image of a three-sided grain with the special boundaries in red and the general boundaries in black. By changing the low-angle boundary threshold,  $\Theta_{LA}$ , the classification of the quadruple node changes as well.

Figure 12: Fraction of special boundaries,  $p$ , as a function of the low angle threshold,  $\Theta_{LA}$ .

Figure 13: Fraction of special boundaries,  $p$ , as a function of the Brandon prefactor,  $\Theta_{CSL}$ .

Figure 14: The quadruple node distribution for aluminum. The population of each particular quadruple node,  $Q_{ij}$ , is given as a function of the global fraction of special boundaries,  $p$ . The blue points are the experimental data from this work, the red curves are for a randomly assembled network (Eq. (3)), and the green and purple curves are from simulations done by Frary and Schuh [19] for fiber textured and general textured microstructures, respectively.

Figure 15: The quadruple node distribution for copper. The population of each particular quadruple node,  $Q_{ij}$ , is given as a function of the global fraction of special boundaries,  $p$ . The blue points are the experimental data from this work, the red curves are for a randomly assembled network (Eq. (3)), and the yellow curve is from simulations done by Frary and Schuh [19] for a twinned microstructure.

## 1. Introduction

Grain boundaries are known to play a role in many material properties, including corrosion [1] and fracture mechanics [2]. Understanding the character and structure of each grain boundary is important because some boundaries exhibit “special” properties such as resistance to cracking or corrosion. In cubic crystals, each grain boundary is described formally by five macroscopic degrees of freedom which can be used to characterize the boundary [3]. However, when classifying all of the boundaries in a microstructure, it is hard to manage these five parameters; therefore, it is more common to use a binary classification. In these binary classification systems, each grain boundary is classified as either “special” or “general” based on its structure. These classifications often coincide with the beneficial or detrimental properties that the boundaries exhibit. For example, a crack would not propagate along a special boundary while it would along a general boundary. Two very common classification systems are: (1) low-angle vs. high-angle boundaries, based on misorientation angle only, and (2) coincidence site lattice (CSL) vs. non-CSL boundaries. In this project, aluminum microstructures are studied in the framework of the former, while copper microstructures are considered using the latter.

In the first classification system, the misorientation angle is determined by bringing the crystal lattice of one grain into coincidence with another grain, finding the common axis between the lattices, and then finding the rotation about this common axis required to bring the two crystal lattices into coincidence [4]. Here, grain boundaries are classified as special if their misorientation angle is less than a threshold value,  $\Theta_{LA}$ . Each different property may have a different low-angle threshold below which the grain boundaries exhibit special properties. The threshold angle is property specific, but is often less than  $15^\circ$ . Superconductivity is a property

that is significantly affected by low-angle boundaries [5], along with diffusion, which is slowed because low-angle boundaries have less free volume [6].

The second classification system is based on the coincidence site lattice model which assigns a  $\Sigma$  number to boundaries that have a some degree of atomic matching [7]. For example, if two grains with cubic symmetry are rotated  $38.67^\circ$  about a [100] axis with respect to one another, one in five lattice points coincide and the boundary between them is considered a  $\Sigma 5$ . Although high  $\Sigma$  values are possible, only boundaries with low  $\Sigma$  numbers ( $\Sigma \leq 29$ ) exhibit special properties [3, 8] and these are referred to as the “special” boundaries. Although a boundary with a low  $\Sigma$  number has a high degree of atomic matching, the boundary misorientation is not always identical to the ideal CSL misorientation. In this case, the boundary will be classified as a CSL boundary if its deviation is within a certain threshold as governed by Brandon’s criterion [9], which states:

$$\Theta_{\max} = \Theta_{\text{CSL}} \Sigma^{-1/2} \quad (1)$$

where  $\Theta_{\max}$  is the maximum allowable angular deviation and  $\Theta_{\text{CSL}}$  is a prefactor in the equation. The prefactor  $\Theta_{\text{CSL}}$  is commonly taken as  $15^\circ$  such that the allowable deviation of  $\Sigma 1$  (low-angle) boundaries corresponds to  $\Theta_{\text{LA}}$ . However,  $\Theta_{\text{CSL}}$  can be changed to give a higher or lower threshold for maximum deviation.

Given that some grain boundary structures exhibit “special” properties, it is desirable to have a large fraction of special boundaries in a microstructure. While special boundaries occur naturally in all polycrystalline materials, certain processing techniques—known as “grain boundary engineering”—can control the fraction of special boundaries,  $p$ , in the microstructure

[10,11]. By increasing the special fraction, more of the grain boundaries will be resistant to damage, leading to an overall improvement in properties [12,13]. In order to monitor the evolution of the special fraction during grain boundary engineering, it is necessary to quantitatively determine the character of each boundary. Transmission Electron Microscopy (TEM) has long allowed for the quantitative measure of grain boundary structure. However, only a small number of grain boundaries can be measured due to the small sample sizes and time-intensive procedure. More recently, Scanning Electron Microscopy (SEM) techniques, including Electron Back-Scattered Diffraction (EBSD) and Orientation Imaging Microscopy (OIM, a trademark of TSL, a division of EDAX) have allowed for advances in rapid grain boundary characterization [14]. In EBSD, a stationary electron beam strikes a polycrystalline sample tilted at  $70^\circ$  and the diffracted electrons form a pattern on a fluorescent screen that is characteristic of the crystal structure and orientation of the sample region from which it was generated. The beam is scanned on a grid across a polycrystalline sample and the crystal orientation measured at each point. The computer program, Orientation Imaging Microscopy, interprets the diffraction data then calculates the Euler angles for each grain and the misorientation of every grain boundary. Using this data, OIM can then create a map that reveals the constituent grain morphology and orientations (Figure 1a). The different colors correspond to different grain orientations as indicated in the inverse pole figure below the OIM scan. To get an idea of how quickly OIM can scan a relatively large area, Figure 1a shows a scan that is 585 x 857 microns. The step size was 9 microns and 7271 points were collected in approximately 40 minutes. Figure 1b shows that same area, but with only the grain boundaries shown. The ability to characterize the grain boundaries with this program allows microstructures to be analyzed very easily.

Through the use of these new techniques, the study of grain boundaries can move beyond individual grain boundaries and towards the consideration of how the individual grain boundaries are connected within a microstructure. This larger system is referred to as the grain boundary network (see Figure 1b). The connectivity of grain boundaries in two dimensions is dependent on features called triple junctions, the points where three grain boundaries meet. Figure 2 shows a schematic grain boundary network where the grains are all six-sided, the lines represent the grain boundaries, and the vertices are the triple junctions. The importance of the triple junctions can be better understood by considering an example. In Figure 2, the green lines represent special boundaries and the red lines represent a crack moving across the microstructure along the general grain boundaries. At the triple junction circled in blue, the crack is arrested by the presence of two special boundaries, illustrating that the presence of the special (i.e., crack-resistant) boundaries at triple junctions can improve the properties of a material. The coordination of special boundaries at triple junctions can be quantified using the triple junction distribution (TJD), a measure of the probability of finding a particular type of triple junction based on the special boundary fraction of a material. The TJD gives  $J_i$ , the fraction of junctions coordinated by  $i$  ( $= 0, 1, 2, \text{ or } 3$ ) special boundaries. Figure 3 shows the four different types of triple junctions, with the special boundaries in green and the general boundaries in maroon. Since certain triple junctions are effective in improving material properties (i.e., the  $J_2$  arrested crack growth in Figure 2), a quantitative measure of the triple junction populations is desired to further understand how material properties are affected by coordination and connectivity of boundaries. In a random network, where all of the boundaries have an equal probability of being special, the TJD is given by a straightforward probabilistic argument [15]:

$$J_0 = (1 - p)^3, \quad (2a)$$

$$J_1 = 3p(1 - p)^2, \quad (2b)$$

$$J_2 = 3p^2(1 - p), \quad (2c)$$

$$J_3 = p^3. \quad (2d)$$

The black curves in Figure 4 show the distribution predicted by Eq. (2). Figure 4 also shows the TJDs from existing experimental data obtained and presented by other researchers, and results from simulations done by Frary and Schuh [15]. The TJDs from both experiments and simulations do not follow the expected random distribution as evidenced by the population of  $J_2$  junctions being below the random expectation and the population of  $J_3$  junctions being above the expected value. In addition to Frary and Schuh, other authors have used the TJD to measure local connectivity [16,17] and have also found that real microstructures do not follow the distribution as predicted by Eq. (2). Instead, grain boundary networks have been found to be non-random as a result of crystallographic constraints at each triple junction, which promote preferential coordination of special boundaries [18]. If the coordination of special boundaries at triple junctions is non-random, there could be long-range implications on the overall connectivity of special boundaries in the network.

The connectivity of grain boundary networks in two dimensions is well understood through the non-random TJD. However, it is important to determine how the crystallographic constraints that led to the non-random TJD impact the connectivity of grain boundaries in three dimensions. This can be done by investigating “quadruple nodes,” a feature in three-dimensional (3D) microstructures. A quadruple node is the point in a three-dimensional microstructure where four

grains, six grain boundaries, and four triple junctions meet, as shown in Figure 5a. The grains are modeled as 14-sided tetrakaidecahedra and are labeled  $G_0$  through  $G_3$ . The shared faces are the grain boundaries and three of these are labeled a, c, and f in Figure 5a. In Figure 5b, the grain boundaries are labeled a-f and the thick black lines represent the triple junctions. It is hard to visualize the quadruple node in 3D and for this reason the schematic in Figure 5c is used to represent the quadruple node. The grains in Figure 5c have the same shading as the grains in 5a and are represented by the enclosed areas within the triangle and the entire area outside of the triangle. The lines are boundaries and the vertices are triple junctions.

In three dimensions, the grain boundary network connectivity is dependent on special boundary coordination at quadruple nodes just as connectivity in two dimensions is dependent on coordination at triple junctions. Analogous to the way a triple junction is classified, quadruple nodes can also be classified based on the number of special boundaries in each node. However, because quadruple nodes exhibit isomerism, it is insufficient to classify quadruple nodes on the basis of their special boundary composition alone [19]. For example, two quadruple nodes with the same boundary composition (e.g., both having four of six special boundaries) can be topologically unique because of the way the special boundaries are arranged amongst the six boundaries [19]. When the topology of the quadruple node is taken into account, eleven different quadruple nodes are possible, as illustrated in Figure 6. Each quadruple node is labeled  $Q_{ij}$ , where  $i$  (= 0 to 6) is the number of special boundaries (green lines) in the quadruple node and  $j$  (= 0 to 4) is the number of triple junctions that have at least two special boundaries. It is then possible to create a quadruple node distribution (QND) which gives a statistical measure of local

connectivity in 3D. The distribution of quadruple node types in a random network is given by a straightforward probabilistic argument [19]:

$$Q_{00} = (1 - p)^6 \quad (3a)$$

$$Q_{10} = 6p(1 - p)^5 \quad (3b)$$

$$Q_{20} = 3p^2(1 - p)^4 \quad (3c)$$

$$Q_{21} = 12p^2(1 - p)^4 \quad (3d)$$

$$Q_{31} = 4p^3(1 - p)^3 \quad (3e)$$

$$Q_{32} = 12p^3(1 - p)^3 \quad (3f)$$

$$Q_{33} = 4p^3(1 - p)^3 \quad (3g)$$

$$Q_{43} = 12p^4(1 - p)^2 \quad (3h)$$

$$Q_{44} = 3p^4(1 - p)^2 \quad (3i)$$

$$Q_{54} = 6p^5(1 - p) \quad (3j)$$

$$Q_{64} = p^6. \quad (3k)$$

In prior work done to quantify non-random quadruple node distributions, Frary and Schuh simulated a variety of microstructures that they called fiber textured, general textured, and twinned [19]. The fiber textured simulations were created by individually rotating all grains randomly within a prescribed tolerance about a shared, high symmetry axis, while the general textured simulations used the same procedure but rotated the grains about a randomly selected axis. In both cases, the grain boundaries were then classified as low- or high-angle boundaries based on their misorientation angle alone. In the present work, these simulation results will be compared to the experimental QND for aluminum. The twinned microstructure was created by

randomly selecting each individual grain and rotating them through different  $\Sigma 3$  transformation variants at random, creating many  $\Sigma 3^n$  boundaries. In the present work, these simulation results will be compared to the experimental QND for copper.

## **2. Method for Obtaining Quadruple Node Information from 2D Sections**

Although there are some methods for obtaining 3D microstructural data such as 3D X-Ray Diffraction [20] and serial sectioning [21], one of the goals of this project is to obtain 3D data (in the form of the QND) from 2D sections using a newly developed approach as illustrated in Figure 7. If a material is sectioned normal to the dotted line in Figure 7a at the red dot (just above the quadruple node), the resulting surface should reveal the triple junction composed of grain boundaries a, b, and c as shown in Figure 7b. In Figure 7b, the colors of the grains match those in Figures 5a and 5c. If the quadruple node is then sectioned normal to the dotted line at the purple dot in Figure 7d (just below the quadruple node), grain  $G_3$  will appear as a triangle with grains  $G_0$ ,  $G_1$ , and  $G_2$  surrounding it (Figure 7e). Figures 7c and 7f show the same region in a copper sample (the blue lines outline the same grains in both pictures) where after polishing to a depth of approximately 15 microns, the triple junction highlighted in Figure 7c has given rise to the three-sided grain in Figure 7f. Following this example, it is expected that three-sided grains that appear in a microstructure are either just above or just below a quadruple node. Using this assumption, it is reasonable to investigate three-sided grains to get information about quadruple nodes.

### **3. Experimental Procedure**

The goal of the project was obtain an experimental quadruple node distribution. To do this, both commercially pure aluminum and commercially pure copper were analyzed and their grain boundary character around three-sided grains was determined.

#### **3.1 Specimen Preparation**

The aluminum was from a rod purchased from Alfa Aesar and the copper was from a bar of unknown origin. These materials were chosen to have either few (Al) or many (Cu) twin boundaries. To prepare the samples, a small piece of each material was mounted in a conductive copper mount, grinded on silicon carbide papers to 800 grit, and then polished with 1 micron and 0.3 alumina suspension. The polishing was finished by using colloidal silica.

Following the polishing steps, a pattern of four fiducial markers was made on the surface using a Vicker's Hardness tester in order to identify different sections of the sample. Finally, a last sample preparation step was applied separately to each sample. For aluminum, the sample was anodized for 1 minute at 31 volts in a 3% fluboric acid solution at room temperature. The sample was then placed a 185°F solution of 35mL of phosphoric acid and 20 grams of chromium trioxide in 1 liter of deionized water for 3 minutes for stripping, which reveals the microstructure. For copper, the sample was electropolished at 15 volts for 5 seconds in a 90% methanol, 10% nitric acid solution at room temperature.

With the microstructure of each material revealed, optical micrographs were taken with the fiducial markers in full view (Figure 8). From there, it was possible to keep track of individual

grains within the material by identifying which marker was nearby. In Figure 8, three indents are visible in an optical micrograph of copper, and are labeled 1 through 3. Figure 8 also shows some three-sided grains, which are outlined in black and labeled a through d. The microstructure of aluminum is shown in Figure 9 where the three-sided grains are circled in yellow and labeled a through c. Once the three-sided grains were identified, the position of each was recorded in relation to the fiducial markers. After finding several three-sided grains in the optical micrograph, EBSD, which is attached to a Phillips XL30 Environmental SEM, was used to characterize the misorientation of the grain boundaries associated with each three-sided grain. Each three-sided grain that was located in the optical micrographs was found in the SEM and an EBSD scan was performed on the area surrounding the three-sided grain. Figure 10 shows an OIM scan of a three-sided grain in copper with each color in the figure representing different orientations indicated by the inverse pole figure. The black lines indicate the position of the grain boundaries; these lines are jagged because OIM data is collected on a hexagonal grid. The data in Figure 10 represents a typical scan done on a three-sided grain using a step size of 2 to 4 microns to collect 1800 to 2000 points in 10 minutes.

After the scans were completed, the grain boundaries were characterized in OIM using a built-in tool that calculates the relative misorientation between two user-selected points. For each of the six grain boundaries associated with the three-sided grain, the misorientation angle for aluminum and the  $\Sigma$  value and deviation angle for copper were recorded. The grain boundary character was measured at an average of five spots along the grain boundary and the average deviation was recorded. Data for 100 aluminum three-sided grains and 102 copper three-sided grains were obtained.

### 3.2 Analysis of Quadruple Nodes

A data set for a wide range of special fractions was desired in order to get a meaningful quadruple node distribution. Although a single specimen was used in this study, the fraction of special boundaries could be adjusted through the definition of  $\Theta_{LA}$  or  $\Theta_{CSL}$ . For example, if  $\Theta_{LA} = 50^\circ$ , the special fraction will be very high because most of the grain boundary misorientations are below that threshold. However, if  $\Theta_{LA} = 1^\circ$ , the special fraction will be very low because most of the grain boundary misorientations exceed that value. By incrementally changing  $\Theta_{LA}$ , a quadruple node distribution for a wide variety of special fractions in aluminum can be obtained. Similarly, changing  $\Theta_{CSL}$  in Eq. (1) alters the special fraction and a quadruple node distribution can be obtained for copper. This approach is illustrated in Figure 11, where the same quadruple node is analyzed for  $\Theta_{LA} = 10^\circ, 30^\circ, \text{ and } 50^\circ$ . The black and red lines are the general and special boundaries, respectively. As Figure 11 shows, when  $\Theta_{LA} = 10^\circ$ , only two of the boundaries are special ( $\Theta_x < \Theta_{LA}$ ), resulting in the classification of this quadruple node as  $Q_{21}$ . In contrast, when  $\Theta_{LA} = 50^\circ$ , all of the boundaries are special and the quadruple node is classified as  $Q_{64}$ . The procedure for obtaining the QND in aluminum works as follows and was implemented in a computer algorithm. First, a value of  $\Theta_{LA}$  is chosen and, for each quadruple node, all six grain boundaries are classified as either special or general. Next,  $Q_{ij}$  is found by determining how many special boundaries are in the specific quadruple node and how many triple junctions contain at least two special boundaries. From all 100 quadruple nodes, the special fraction can be found using:

$$p = \frac{1}{6}(Q_{10}) + \frac{2}{6}(Q_{20} + Q_{21}) + \frac{3}{6}(Q_{31} + Q_{32} + Q_{33}) + \frac{4}{6}(Q_{43} + Q_{44}) + \frac{5}{6}(Q_{54}) + \frac{6}{6}(Q_{64}). \quad (4)$$

The same procedure was used for copper by changing  $\Theta_{\text{CSL}}$ . For aluminum,  $\Theta_{\text{LA}}$  was changed from  $1^\circ$  to  $50^\circ$  which changed  $p$  from 0 to 0.95. For copper,  $\Theta_{\text{CSL}}$  in Eq. (1) was changed from  $1^\circ$  to  $15^\circ$  by increments of  $2^\circ$ , resulting in special fractions between 0 and 0.35. This lower special fraction is a result of the fact that  $\Theta_{\text{CSL}}$  in Eq. (1) has a practical upper bound of  $15^\circ$ . Figures 12 and 13 show how  $p$  varies with  $\Theta_{\text{LA}}$  or  $\Theta_{\text{CSL}}$ .

#### 4. Discussion

Using the procedures described in the previous section, an experimental QND has been obtained as shown in Figures 14 and 15 along with the QNDs of a random microstructure and relevant simulated microstructures described above. These figures show the population of each particular quadruple node as a function of the global fraction of special boundaries. The blue points are the experimental data from this work, the red curves are for a randomly assembled network (Eq. (3)), and the green, purple and yellow curves are the simulation results. Note that the y-axes in Figure 15 are not the same for each graph so as to reveal more detail in each curve.

In these figures, it is expected that the experimental QND for each material will match the relevant simulations more closely than the random microstructure. However, it is more significant to the goal of this project to look at whether the microstructure is random or non-random and to weigh that conclusion more heavily than whether the experimental QND matches any of the relevant simulations. In looking at each graph, it is important to understand that each blue data point represents all 100 aluminum or all 102 copper three-sided grains evaluated at a particular value of  $\Theta_{\text{LA}}$  or  $\Theta_{\text{CSL}}$ , respectively.

## 4.1 Analysis of Aluminum

Looking more closely at the individual quadruple node populations for aluminum shown in Figure 14, they often fall into one of three categories:

- 1) *The experimental data matches very well to one of the simulated microstructures.* For example, both  $Q_{00}$  and  $Q_{10}$  match the fiber textured simulation very well. This suggests that the special boundaries coordinate preferentially about the quadruple nodes as a result of crystallographic constraints.
- 2) *The experimental data is distinctly non-random and lies between the quadruple node distributions of the simulated microstructures.* For example, the population of  $Q_{31}$  nodes in the simulated microstructure is predicted to be much higher than in a random network. While the experimental data does not follow either the fiber or general textured simulations very well, the experimental data is definitely above that of the random line. In the  $Q_{32}$  graph, the fiber and general textured simulations predict that the experimental QND will be below that of the random QND, and the experimental data follows this trend. Also, the experimental populations of  $Q_{44}$  and  $Q_{64}$  nodes match closely to the simulated microstructures.
- 3) *The simulated microstructures match too closely to the random network expectations to distinguish non-random behavior.* This is the case for  $Q_{20}$ , where the general textured simulation and the random curves overlap.

## 4.2 Analysis of Copper

The quadruple node distribution for copper is shown in Figure 15. Due to the fact that the maximum accessible value of  $p$  was 0.35, the results are not as conclusive as for aluminum. However, the resulting quadruple node populations can be described by one of two trends:

- 1) *The experimental data is distinctly non-random.* For example, the population of  $Q_{31}$  nodes in the simulated microstructure is predicted to be much higher than in a random network. While the experimental line does not follow the twinned simulation very well, the experimental data is definitely above that of the random line. In addition, the twinned simulations predict that population of  $Q_{20}$  nodes will be below that of the random QND, and the experimental data follows this trend.
- 2) *The limited range of special fraction sampled does not allow for conclusions.* The special fraction was below 0.35 and therefore did not allow for the dominant features of some quadruple node populations to be revealed. In the cases of  $Q_{44}$ ,  $Q_{54}$ , and  $Q_{64}$ , the populations are zero. However, the populations of those particular quadruple nodes are predicted to be almost non-existent at these low special fractions.

## 4.3 Potential Causes for Scatter in Experimental Quadruple Node

### Distribution

It should be noted that not every graph falls under one of the trends mentioned above. There are several possible explanations for the anomalous behavior observed in some of the quadruple node populations. First, the processing history of either material is not known, so it is unclear how closely either actual material resembles the simulated microstructures. Second, the sample size of approximately 100 points was somewhat small leading to some inconclusive results.

Third, there are two main sources of error in measuring the misorientation angles: (1) inherent error in OIM of approximately  $\pm 1^\circ$ , and (2) scatter encountered when measuring along a boundary, as mentioned above. Any combination of these will make it difficult to obtain a perfect match between the simulations and experimental data.

## **5. Conclusions**

The goal of this project was to extend the study of grain boundary connectivity to three dimensions by finding an experimental quadruple node distribution and comparing it to simulations done by Frary and Schuh [19]. The main findings are summarized below:

1. An experimental procedure was developed to measure the quadruple node distribution from two-dimensional sections. The quadruple node geometry led to a hypothesis in which three-sided grains could be considered to be either just above or just below a quadruple node. From this hypothesis, information about quadruple nodes (and therefore the quadruple node distribution) could be obtained via analysis of three-sided grains.
2. The quadruple node distribution was found to be non-random in aluminum and copper. Although there was a large amount of scatter in the experimental data, a significant number of the quadruple node populations more closely matched those of the simulated microstructures than the random network distribution.

## **6. Future Work**

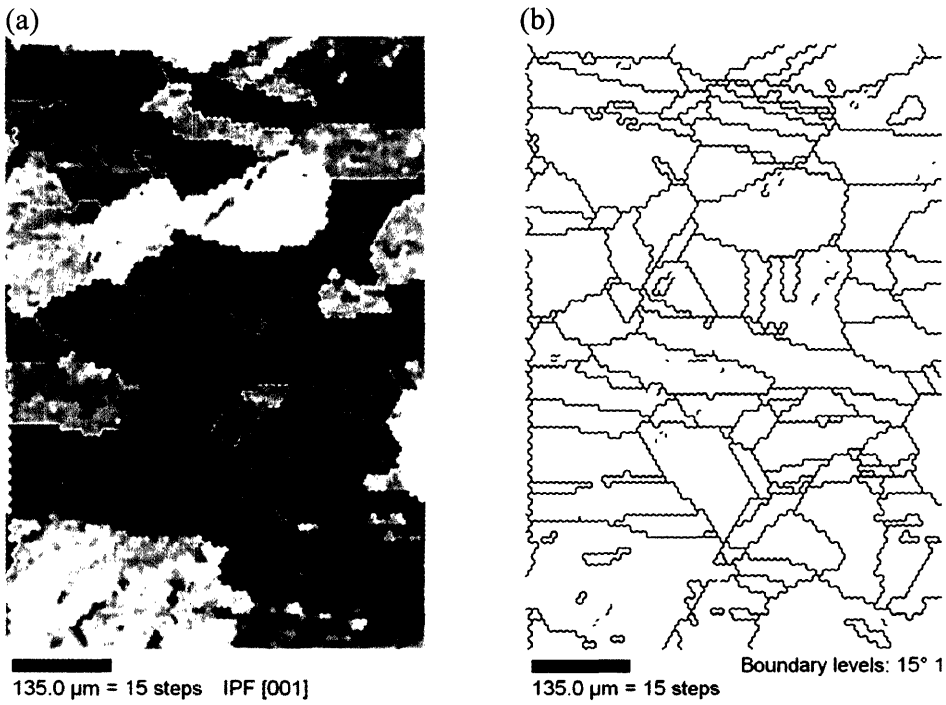
In order to improve the understanding of connectivity in three dimensions, this work could be extended in these ways:

- 1) More data points should be obtained in order to reduce the noise in the results. While approximately 100 points are a significant data set, a larger sample size would smooth the curves and further the understanding of microstructural behavior.
- 2) The use of copper with a higher fraction of twin-related boundaries would allow for more decisive conclusions about the QND for copper. As mentioned above, the QND for copper had a range of  $p$  from 0 to 0.35, which hampered the ability to see some predominant features in certain  $Q_{ij}$  distributions.
- 3) Use the same materials but with different processing conditions in order to see how the QND changes and whether it matches the simulations more closely. The microstructure of the materials used in this project did not necessarily match the simulated microstructures and materials processed in a different way might match the simulated curves more closely.
- 4) A real 3D data set should be obtained and used to get a QND in order to confirm that the results match those discovered in this project, thereby validating the experimental procedure. The experimental QND was found to be non-random but did not match all of the simulated microstructure curves. Investigation into whether this is an artifact of the process would be prudent.
- 5) Verify that it is reasonable to obtain quadruple node information from three-sided grains found in 2D sections. The method used in this project is theoretically sound, but may not be physically true and should be investigated further.

## References

1. Lehockey, E.M., et al., *Mitigating Intergranular Attack and Growth in Lead-Acid Battery Electrodes for Extended Cycle and Operating Life*. Metallurgical and Materials Transactions, 1998. **29A**: p. 387-396.
2. Aust K.T., U. Erb, G. Palumbo, *Interface Control for Resistance to Intergranular Cracking*. Materials Science and Engineering, 1994. **A300**: p. 94.
3. Sutton, A.P. and R.W. Balluffi, *Interfaces in Crystalline Materials*, 1995. Oxford Science Publication.
4. EDAX, *OIM Analysis Users Manual*. www.edax.com, 2001.
5. Hilgenkamp, H. and J. Mannhart, *Grain boundaries in high - $T_c$  superconductors*. Reviews of Modern Physics, 2002. **74**(2): p. 485-549.
6. Peterson, N.L., *Grain-Boundary Diffusion – Structural Effects, Models and Mechanisms*, in *Grain Boundary Structure and Kinetics*. 1979, American Society for Metals: Metals Park, OH. p. 209-238.
7. Grimmer H., W. Bollman, D.H. Warrington, *Coincidence Site Lattices and Complete Pattern Shift Lattices in Cubic Crystals*. Acta Crystallographica, 1974. **A30**: p. 197.
8. Palumbo, G. and K.T. Aust, *Special Properties of Sigma Grain Boundaries*, in *Materials Interfaces*, D. Wolf and S. Yip, Editors. 1992, Chapman and Hall: London. p. 190-211.
9. Brandon, D.G., *The Structure of High-Angle Grain Boundaries*. Acta Metallurgica, 1966. **14**: p. 1479-1484.
10. Watanabe, T., *The Impact of Grain Boundary Character Distribution on Fracture in Polycrystals*. Materials Science and Engineering, 1994. **A176**: p. 39-49.
11. Palumbo, G., E.M. Lehockey, and P. Lin, *Applications for Grain Boundary Engineered Materials*. JOM, 1998. **50**(2): p. 40-43.
12. Shimada, M., et al., *Optimization of grain boundary character distribution for intergranular corrosion resistant 304 stainless steel by twin-induced grain boundary engineering*. Acta Materialia, 2002. **50**(9): p. 2331-2341.
13. Lehockey, E.M. and G. Palumbo, *On the Creep Behavior of Grain Boundary Engineered Nickel*. Materials Science and Engineering, 1997. **A237**: p. 168-172.
14. Wright, S.I., B.L Adams, K. Kunze, *Orientation Imaging: The Emergence of a New Microscopy*. Metallurgical Transactions, 1993. **24A**: p. 819-831.
15. Frary, M., C.A. Schuh, *Percolation and statistical properties of low- and high-angle interface networks in polycrystalline ensembles*. Physical Review B, 2004. **69**: p. 134115.
16. Kumar, M., W.W King, and A.J. Schwartz, *Modifications to the Microstructural Topology in FCC Materials Through Thermomechanical Processing*. Acta Materialia, 2000. **48**: p. 2081-2091.
17. Fortier, P., W.A. Miller, and K.T. Aust, *Triple Junction and Grain Boundary Character Distribution in Metallic Materials*. Acta Materialia, 1997. **45**(8): p. 3459-3467.
18. Schuh, C.A., R.W. Minich, M. Kumar, *Connectivity and Percolation in Simulated Grain Boundary Networks*. Philosophical Magazine, 2003. **A83**(6): p. 711-726.
19. Frary, M., C.A. Schuh, *Connectivity and Percolation Behavior of Grain Boundary Networks in Three Dimensions*. Philosophical Magazine, 2005. **85**: p. 1123-1143.
20. Miao J.W., et al., *High Resolution 3D x-ray diffraction microscopy*. Physical Review Letters, 2002. **89**(8): p. 88303.
21. Enomoto M., *Three-dimensional characterization and analysis of steel microstructure by serial sectioning*. Journal of the Iron and Steel Institute of Japan, 2004. **90**(4): p. 1-7.

## Figures



Color Coded Map Type: Inverse Pole Figure [001]

Copper

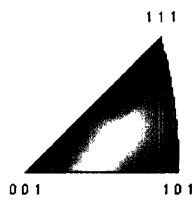


Figure 1: (a) An OIM map of a copper microstructure. The different colors correspond to different grain orientations as indicated in the inverse pole figure below the OIM scan. (b) The same map of a copper microstructure but with only the grain boundaries shown.

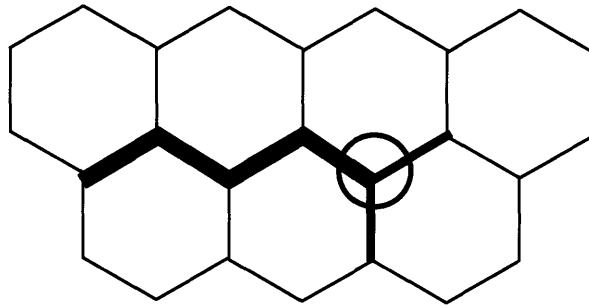


Figure 2: A schematic grain boundary network where each hexagon represents a different grain and each line a grain boundary. A triple junction, the point where three grain boundaries meet, is circled in blue. The green lines highlight the special boundaries and the red lines represent a crack propagating across the grain boundary network. The crack is arrested when it reaches a triple junction with two special grain boundaries.

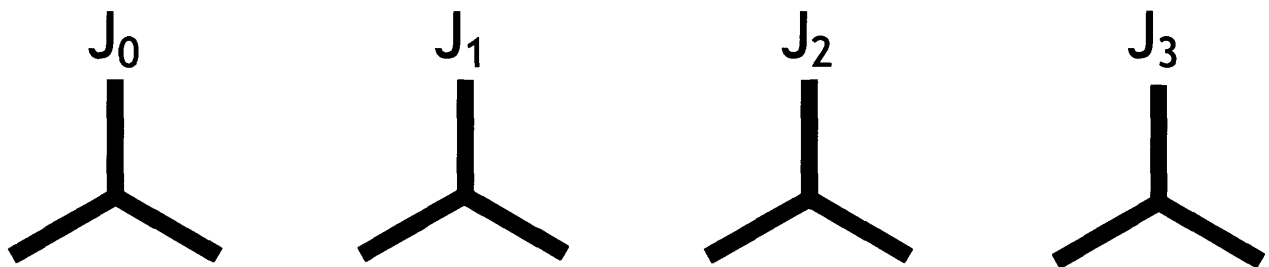


Figure 3: There are 4 different types of triple junctions, classified as  $J_i$ , where  $i$  ( $=0$  to  $3$ ) represents the number of special boundaries in the triple junction. The maroon and green lines represent general and special grain boundaries, respectively.

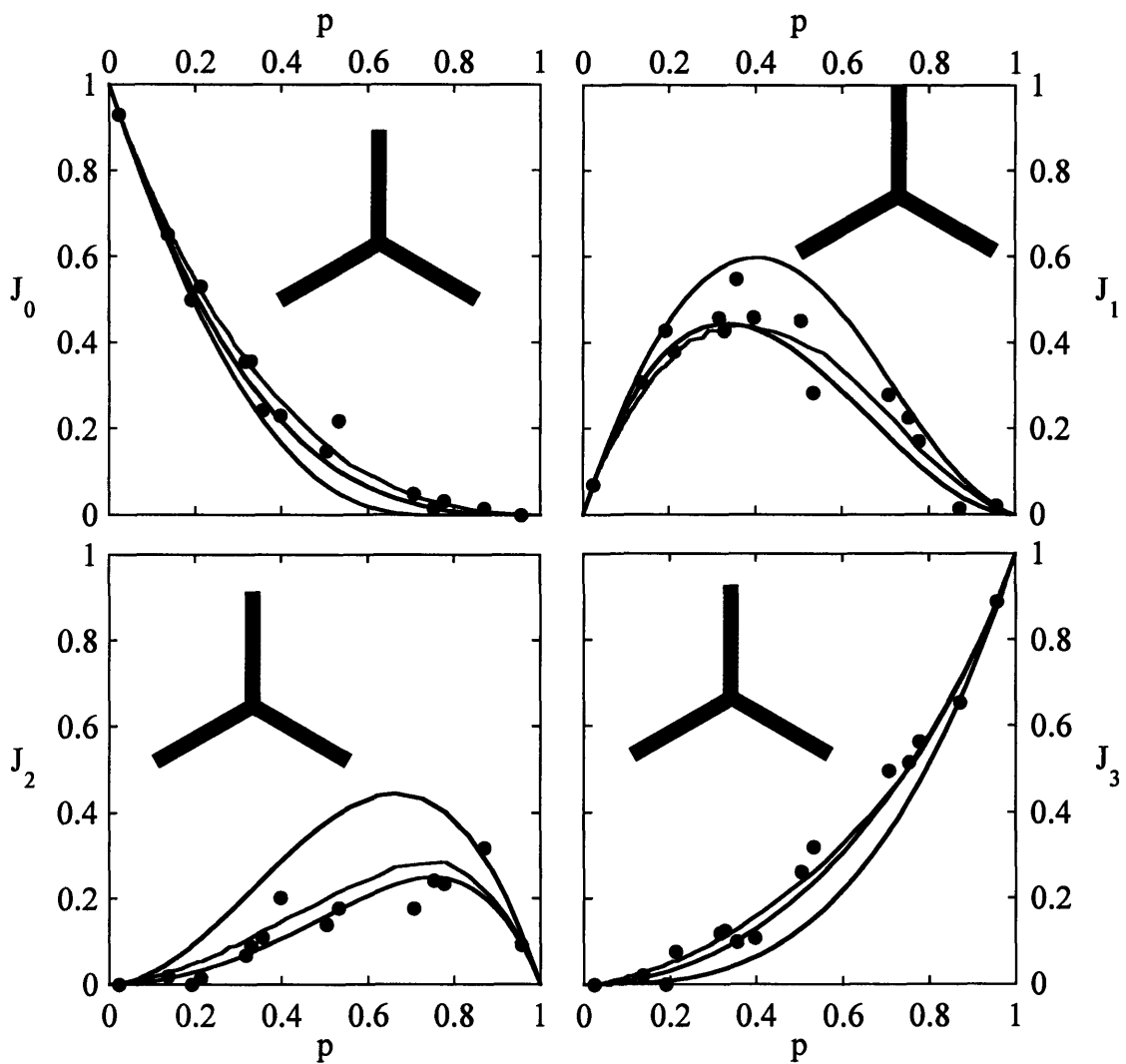


Figure 4: Triple junction distributions as determined by Frary and Schuh for random microstructure (black lines), existing experimental data (points), fiber textured simulations (green), and general textured simulations (purple) [15].

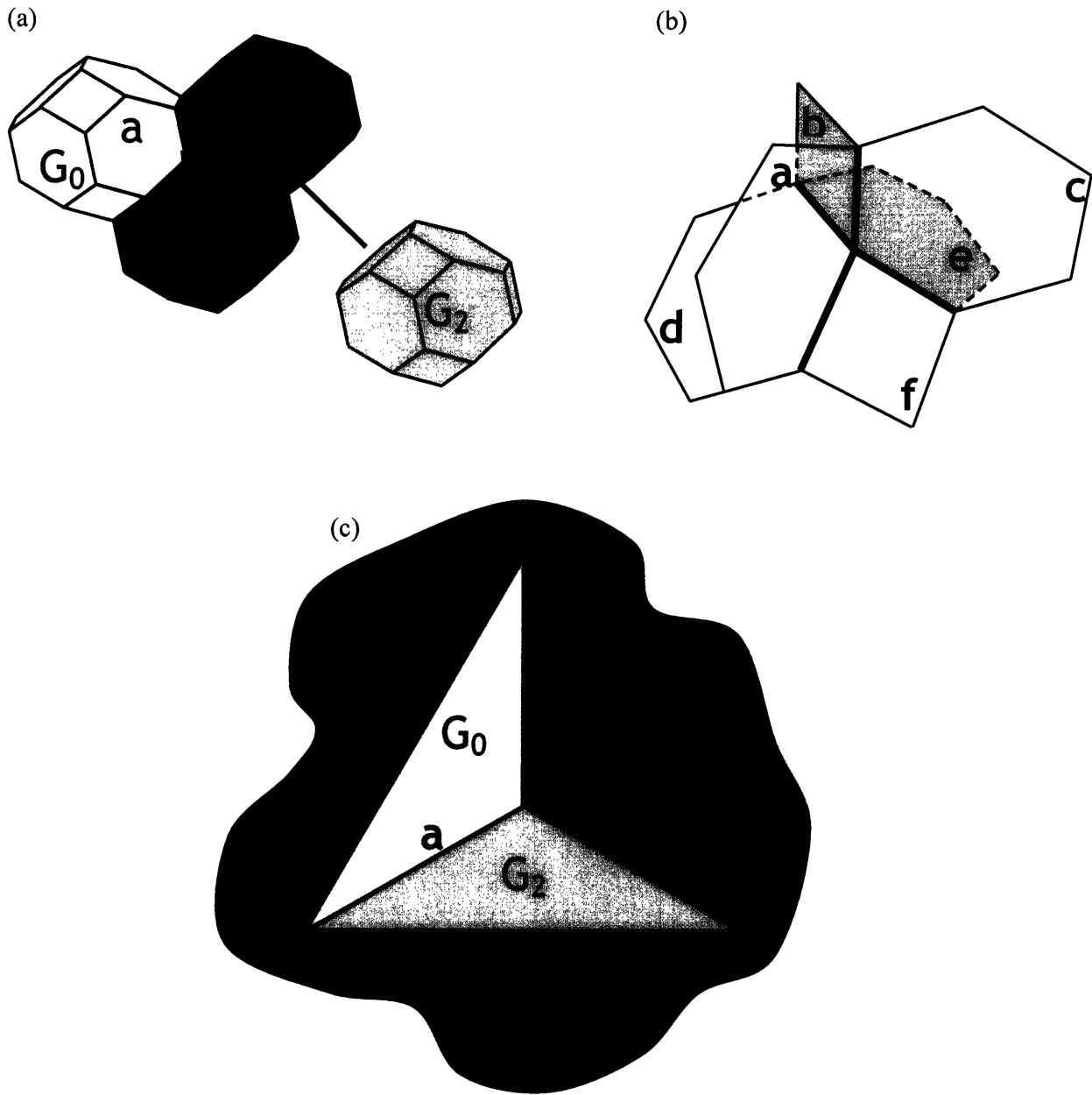


Figure 5: (a) A schematic illustration of a quadruple node, the point where four grains, six grain boundaries, and four triple junctions meet. Each grain is labeled  $G_i$  ( $i = 0$  to  $3$ ) and some of the boundaries are labeled with lower case letters. (b) The same quadruple node as in (a), where the planes (labeled a – f) are the grain boundaries and the thick black lines are the triple junctions. (c) Representation of the quadruple node where the lines are the grain boundaries (labeled a – f) and the vertices are triple junctions. The grains are the areas between the lines; the grain labels and colors are the same as those in part (a).

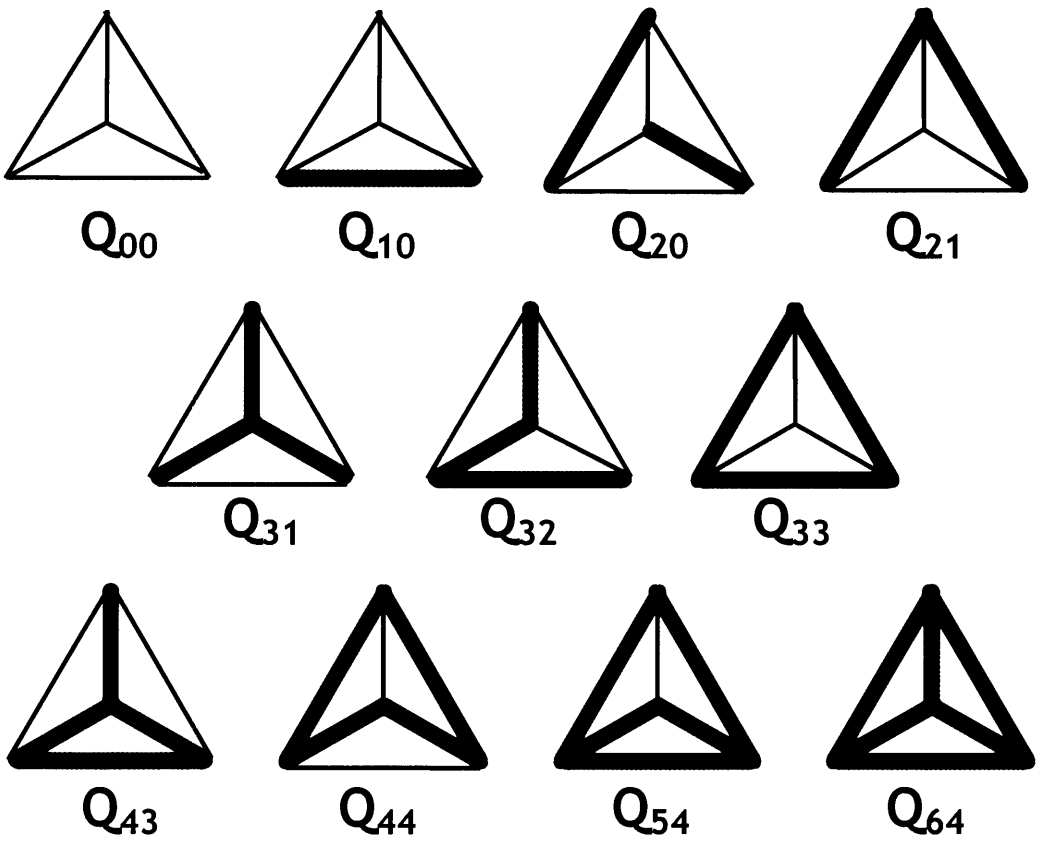


Figure 6: The 11 different types of quadruple nodes, labeled  $Q_{ij}$ , where  $i$  ( $= 0$  to  $6$ ) is the number of special boundaries in the triple junction and  $j$  ( $= 0$  to  $4$ ) is the number of triple junctions coordinated by at least two special boundaries. The thick green lines represent special boundaries while the black lines represent general boundaries.

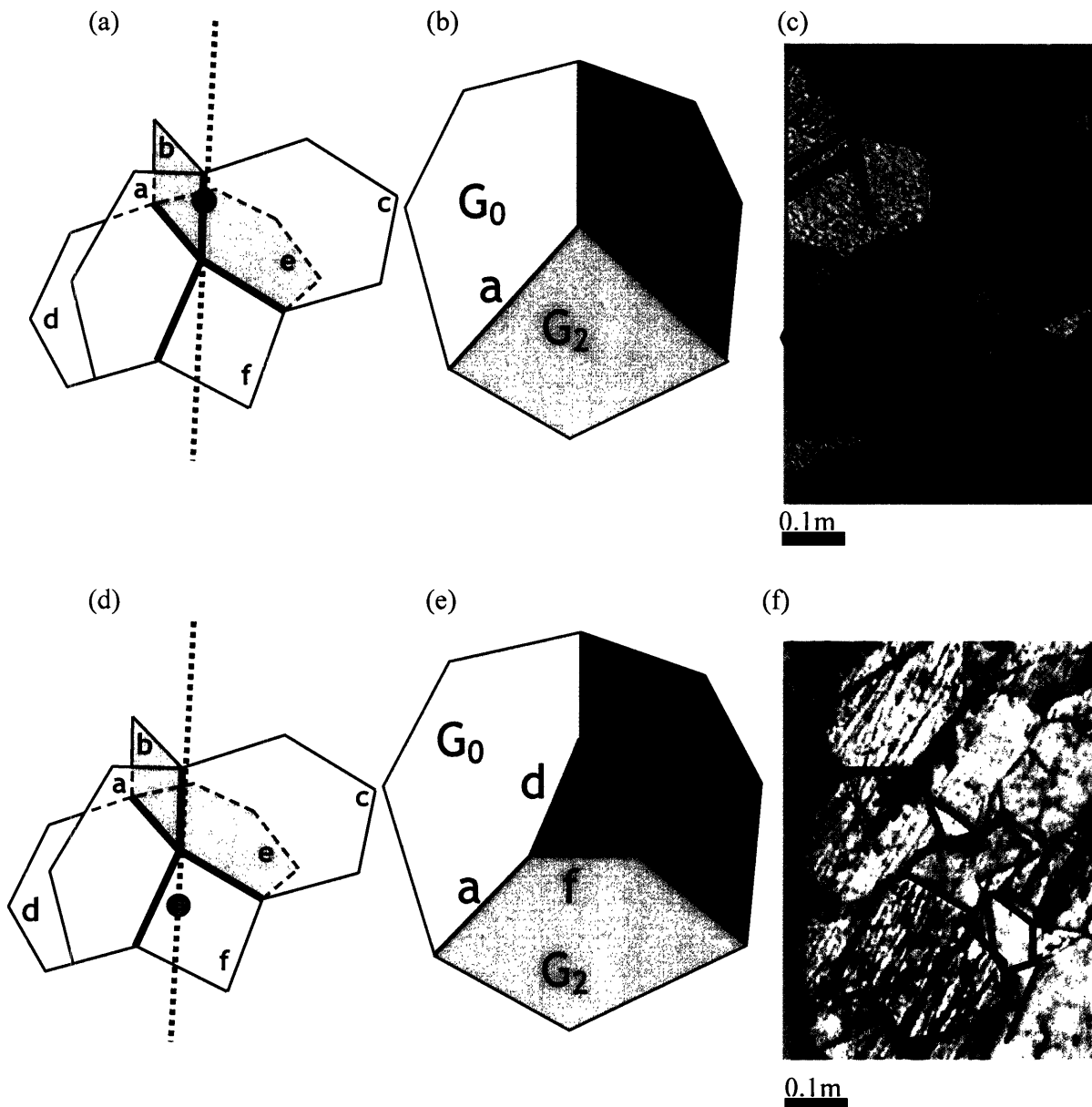


Figure 7: (a) Schematic of a quadruple node shown in Figure 5b. (b) Triple junction formed from grain boundaries a, b, and c. This is what one would see if one sectioned Figure 7a at red dot. (c) Optical micrograph of copper outlined. A triple junction is outlined in green while the blue outlines show other grains in picture. (d) Schematic of a quadruple node shown in Figure 5b. (e) Three sided grain one would see if sectioned Figure 7d at purple dot. (f) The three sided is grain outlined in green while the blue outlines show matching grains from Figure 7c.

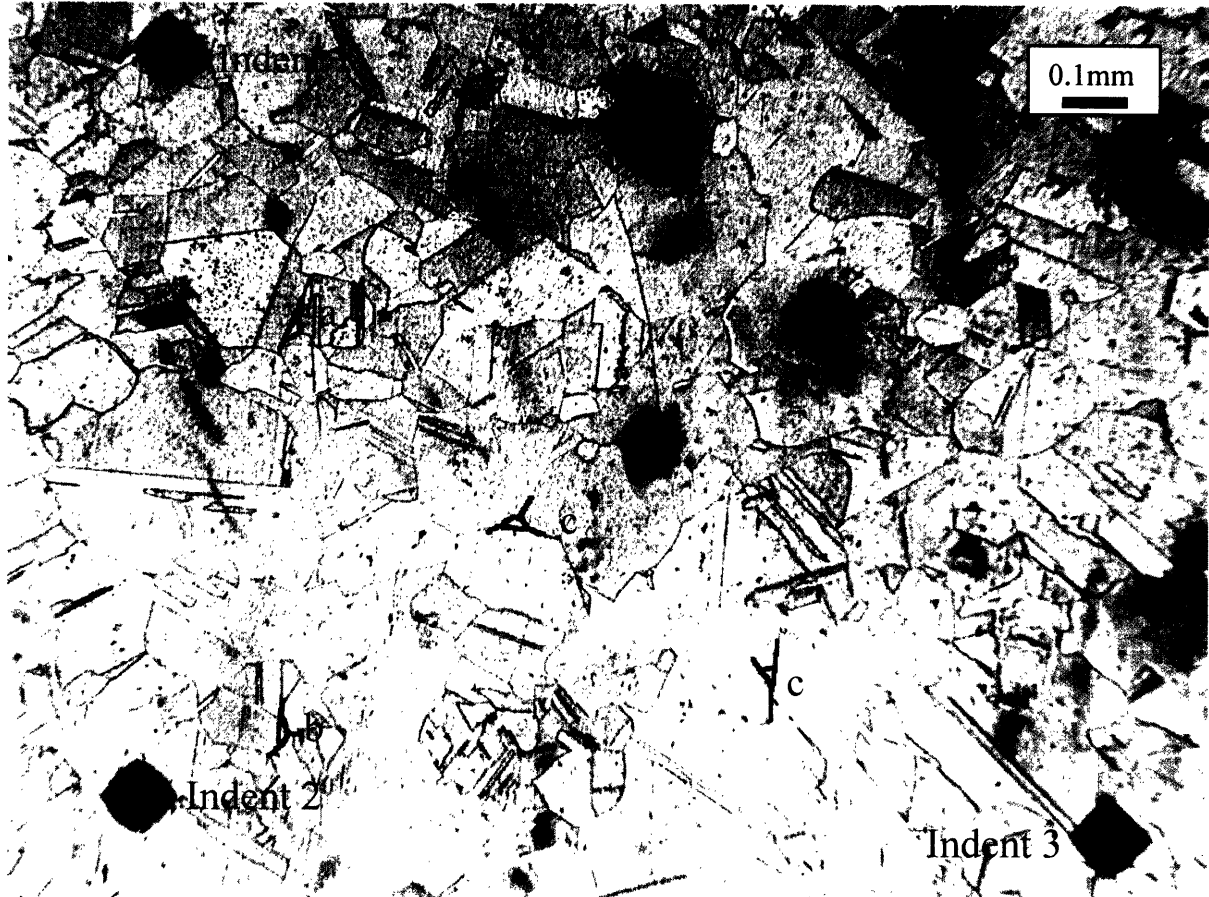


Figure 8: Optical micrograph of copper. The black marks in the corners are Vicker's indents (labeled 1 through 3), which were used as fiducial markers. Several three-sided grains have been identified and are outlined in black (labeled a-d).

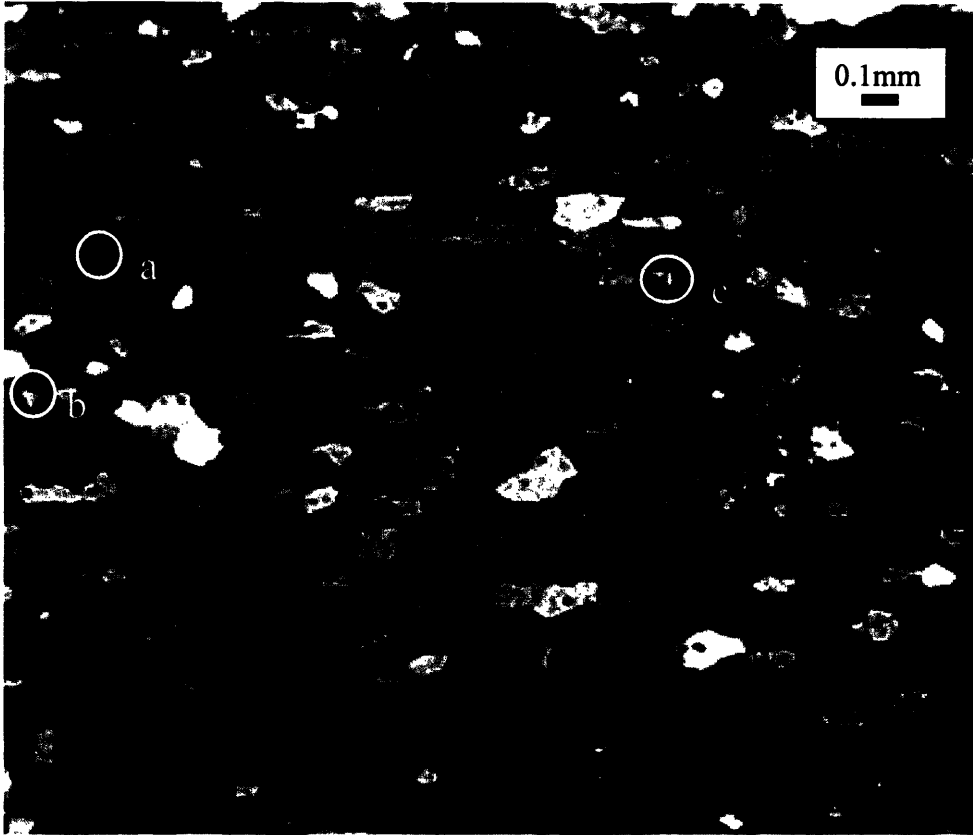


Figure 9: Optical micrograph of pure aluminum. Several three-sided grains have been identified and are circled in yellow (labeled a-c).

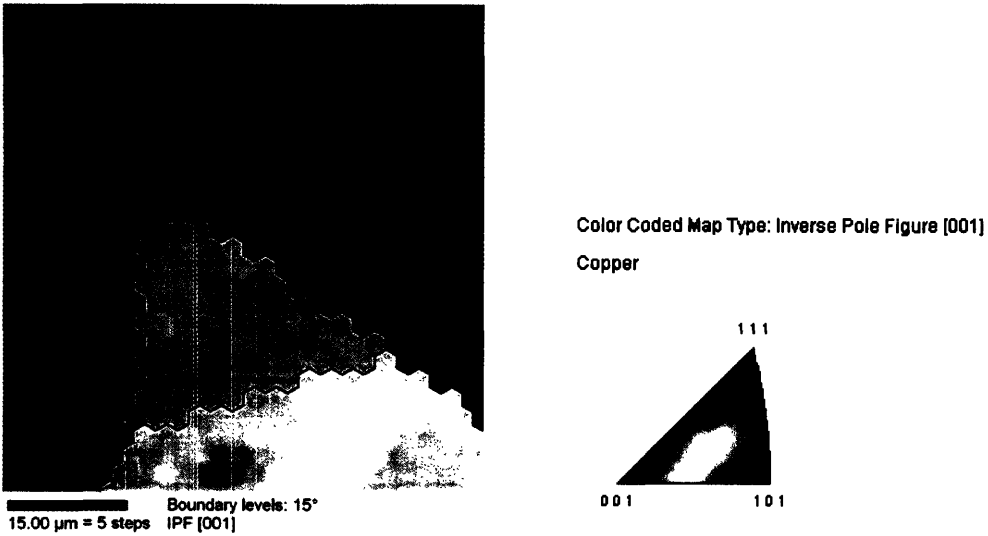


Figure 10: An OIM map of a three-sided grain. The different colors correspond to different grain orientations and are shown in the inverse pole figure beside the OIM scan. A particular point is shaded in the OIM scan according to the alignment of these three directions in the crystal.

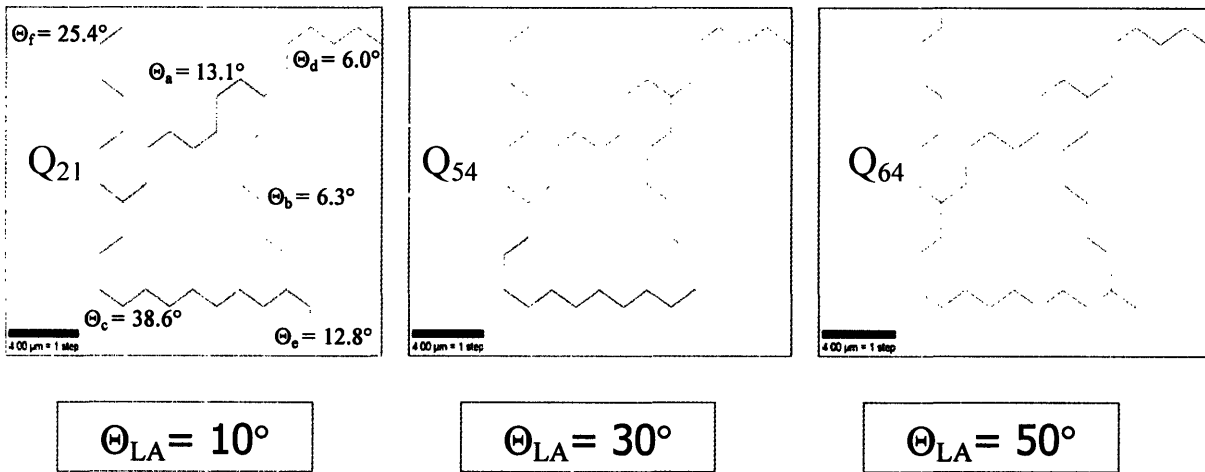


Figure 11: An OIM image of a three-sided grain with the special boundaries in red and the general boundaries in black. By changing the low-angle boundary threshold,  $\Theta_{LA}$ , the classification of the quadruple node changes as well.

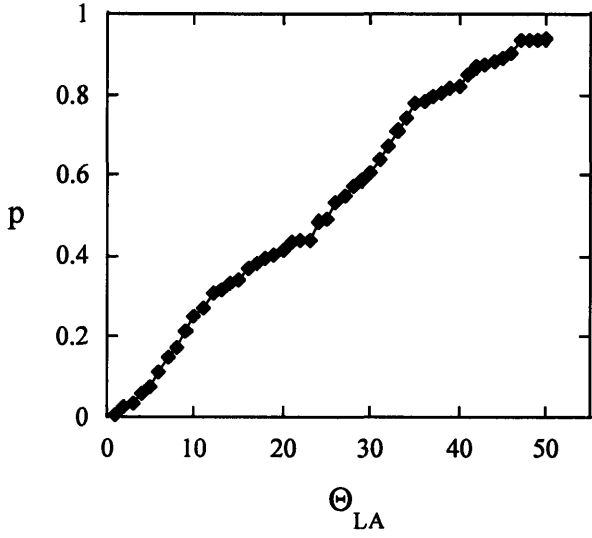


Figure 12: Fraction of special boundaries,  $p$ , as a function of the low angle threshold,  $\Theta_{LA}$ .

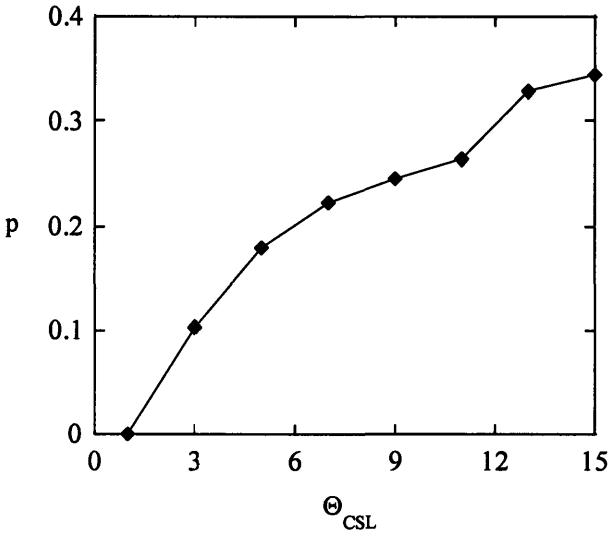


Figure 13: Fraction of special boundaries,  $p$ , as a function of the Brandon prefactor,  $\Theta_{CSL}$ .

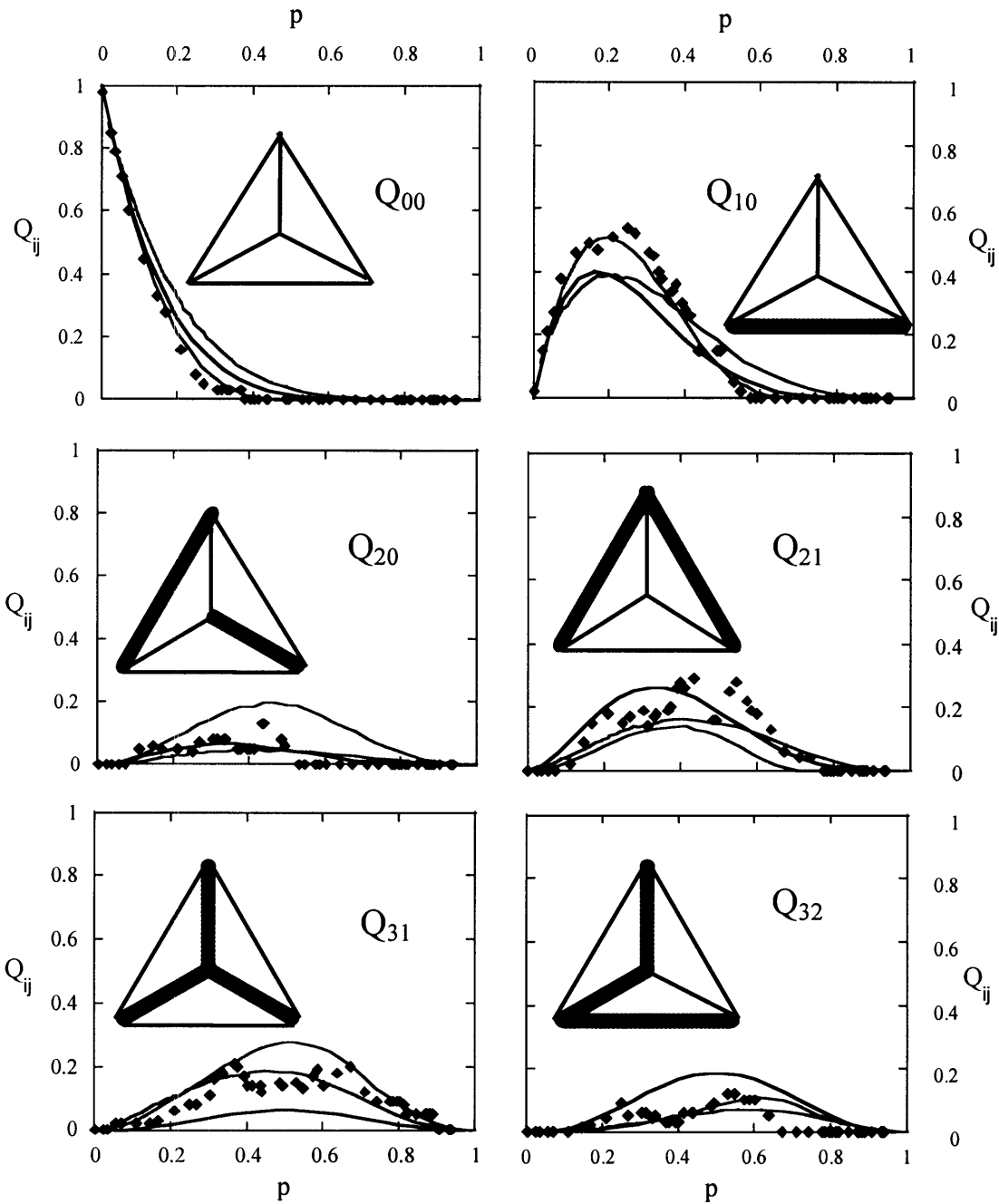


Figure 14: The quadruple node distribution for aluminum. The population of each particular quadruple node,  $Q_{ij}$ , is given as a function of the global fraction of special boundaries,  $p$ . The blue points are the experimental data from this work, the red curves are for a randomly assembled network (Eq. (3)), and the green and purple curves are from simulations done by Frary and Schuh [19] for fiber textured and general textured microstructures, respectively.

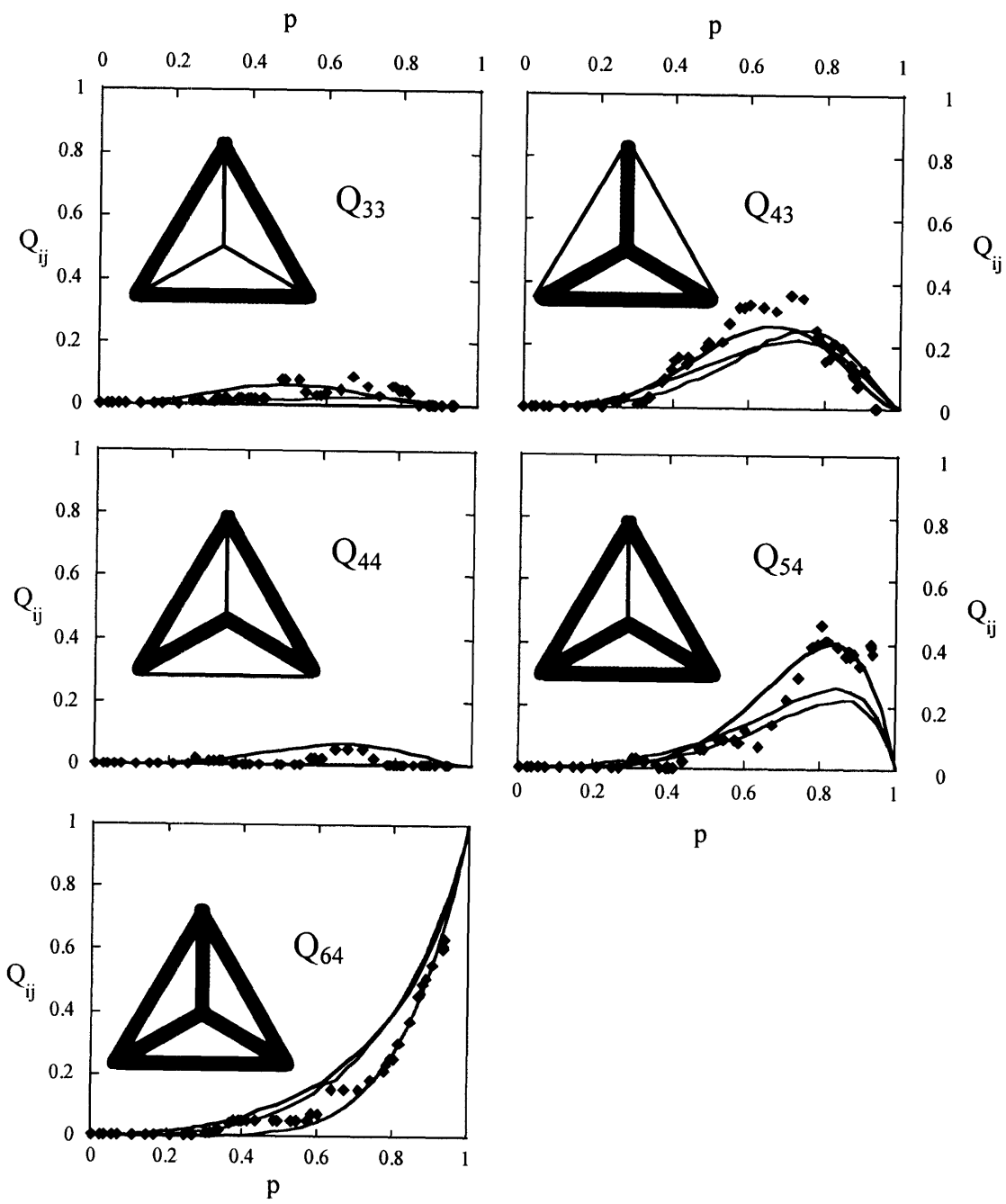


Figure 14 continued.

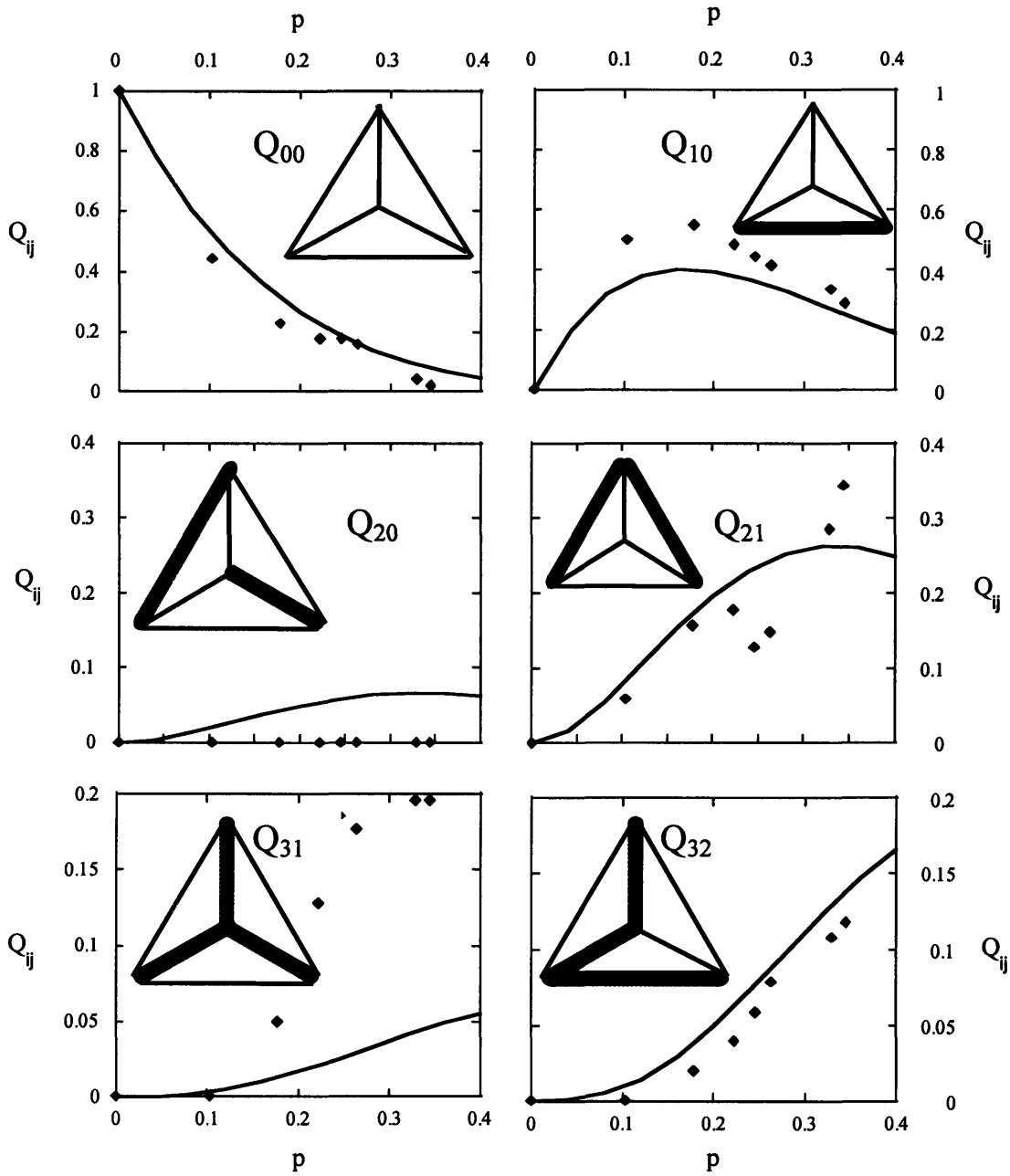


Figure 15: The quadruple node distribution for copper. The population of each particular quadruple node,  $Q_{ij}$ , is given as a function of the global fraction of special boundaries,  $p$ . The blue points are the experimental data from this work, the red curves are for a randomly assembled network (Eq. (3)), and the yellow curve is from simulations done by Frary and Schuh [19] for a twinned microstructure.

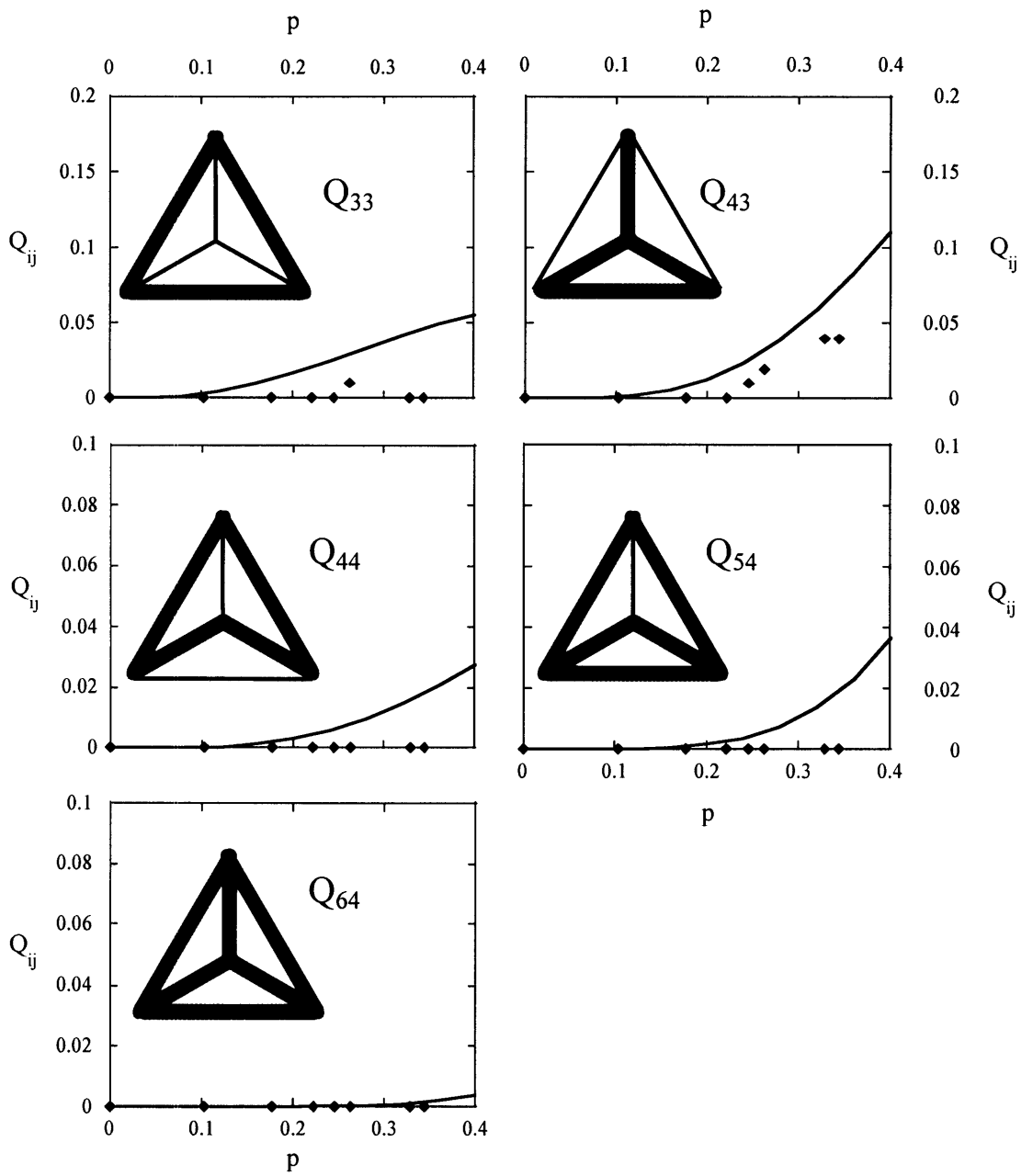


Figure 15 continued.